9-2018

Modulation of Low-Altitude Ionospheric Upflow by Linear and Nonlinear Atmospheric Gravity Waves

M. R. Burleigh
Embry-Riddle Aeronautical University

C. J. Heale
Embry-Riddle Aeronautical University

M. D. Zettergren
Embry-Riddle Aeronautical University

J. B. Snively
Embry-Riddle Aeronautical University, snivelyj@erau.edu

Journal of Geophysical Research: Space Physics

RESEARCH ARTICLE
10.1029/2018JA025721

Modulation of Low-Altitude Ionospheric Upflow by Linear and Nonlinear Atmospheric Gravity Waves

M. R. Burleigh[1], C. J. Heale[1], M. D. Zettergren[1], and J. B. Snively[1]

[1]Department of Physical Sciences, Embry-Riddle Aeronautical University, Daytona Beach, FL, USA

Key Points:
- High-latitude ionospheric upflow can be modulated by thermospheric gravity waves
- *F* region density perturbations due to gravity wave modulations, through heating and cooling processes, modulate the electron temperature
- Increases in electron temperature quickly conduct up the magnetic field lines and drive upflow at altitudes above the initial heating region

Supporting Information:
- Supporting Information S1
- Data Set S1
- Data Set S2
- Data Set S3
- Data Set S4
- Data Set S5
- Data Set S6
- Data Set S7
- Data Set S8
- Data Set S9
- Data Set S10
- Data Set S11
- Data Set S12
- Data Set S13
- Data Set S14

Correspondence to:
M. Burleigh,
burleb34@my.erau.edu

Citation:
Burleigh, M. R., Heale, C. J., Zettergren, M. D., & Snively, J. B. (2018). Modulation of low-altitude ionospheric upflow by linear and nonlinear atmospheric gravity waves. *Journal of Geophysical Research: Space Physics*, *123*, 7650–7667. https://doi.org/10.1029/2018JA025721

Received 25 MAY 2018
Accepted 1 AUG 2018
Accepted article online 9 AUG 2018
Published online 8 SEP 2018

Abstract This study examines how thermospheric motions due to gravity waves (GWs) drive ion upflow in the *F* region, modulating the topside ionosphere in a way that can contribute to ion outflow. We present incoherent scatter radar data from Sondrestrom, from 31 May 2003 which showed upflow/downflow motions, having a downward phase progression, in the field-aligned velocity, indicating forcing by a thermospheric GW. The GW-upflow coupling dynamics are investigated through the use of a coupled atmosphere-ionosphere model to examine potential impacts on topside ionospheric upflow. Specifically, a sequence of simulations with varying wave amplitude is conducted to determine responses to a range of transient forcing reminiscent of the incoherent scatter radar data. Nonlinear wave effects, resulting from increases in amplitude of the modeled GW, are shown to critically impact the ionospheric response. GW breaking deposits energy into smaller scale wave modes, drives periods of large field-aligned ion velocities, while also modulating ion densities. Complementary momentum transfer increases the mean flow and, through ion-neutral drag, can increase ion densities above 300 km. Ionospheric collision frequency (cooling) and photoionization effects (heating), both dependent on ionospheric density, modify the electron temperature; these changes conduct quickly up geomagnetic field lines driving ion upflow at altitudes well above initial disturbances. This flow alters ion populations available for high-altitude acceleration processes that may lead to outflow into the magnetosphere. We have included a representative source of transverse wave heating which, when supplemented by our GWs, illustrates strengthened upward fluxes in the topside ionosphere.

1. Introduction

Ionospheric plasma plays an important role in the coupled magnetosphere-ionosphere-thermosphere system through the conveyance of mass, momentum, and energy from one part of the system to another. Energetic ions from the ionosphere are routinely observed in the magnetospheric plasma sheet and ring current during periods of strong solar wind driving (Klumpar, 1979; Lennartsson et al., 1981; Sharp et al., 1985; Shelley et al., 1972). Studies have indicated that this ionospheric outflow directly affects the dynamic response of the magnetosphere to solar wind variations (Brambles et al., 2011; Garcia et al., 2010; Yu & Ridley, 2013) through a wide range of mechanisms such as mass loading that can affect Alfvén wave and ULF wave propagation (Kozyra et al., 1984), alteration of reconnection rates (Shay et al., 2004), and impacts on the acceleration and loss rates of energetic particles (Daglis et al., 1999; Jordanova et al., 1996).

The most commonly observed processes contributing to ionospheric upflow and outflow are DC electric fields, soft electron precipitation, and gyroresonant wave heating. Strong DC electric fields frictionally heat the ion population resulting in anisotropic increases in ion temperature (St-Maurice & Schunk, 1979) that cause large pressure gradients which push the ions outward and upward (Foster et al., 1998; Keating et al., 1990; Wahlund et al., 1992; Zettergren & Semeter, 2012). Soft electron precipitation heats *F* region electrons creating electron pressure gradients which increase the ambipolar electric field, driving ion upflows (Foster & Lester, 1996; Liu et al., 1995; Ogawa et al., 2000; Wahlund et al., 1992). Velocity shears can also drive ion heating and upflow through lowering the threshold for field-aligned current-driven instabilities to excite ion cyclotron waves at lower altitudes (Ganguli et al., 1994; Liu & Lu, 2004; Nishikawa et al., 1990; Semeter et al., 2003). Upflowing ions may then undergo further acceleration from transverse wave heating by broadband ELF waves (Andre et al., 1998; Kintner et al., 1996; Moore et al., 1999; Whalen et al., 1991). At high altitudes, the mirror force can propel ions to escape velocities, resulting in outflow to the magnetosphere (Moore, 1991). The existence of a multistep ion outflow process such as that described has been suggested by various stud-

ies focusing on coexistence of different energy sources driving outflow (Lynch et al., 2007; Ogawa et al., 2008; Strangeway et al., 2005; Yoshida et al., 1999).

It is well established that the ionosphere can also be modulated by thermospheric winds, which may arise from solar forcing, plasma convection, and/or acoustic gravity waves (GWs; to name a few sources). Neutral winds affect ionospheric motions through collisions (viz., ion-neutral drag) and alter upflow or perpendicular motions, potentially modifying source populations available for secondary acceleration mechanisms (as suggested by Burleigh & Zettergren, 2017). Acoustic GWs (Hines, 1960), which are of primary interest to this study, are often driven at high latitudes by heating produced by auroral electric fields, energetic particle precipitation, and shear forces in the ionosphere (Hocke & Schlegel, 1996). Orographic and weather effects are additional common GW sources (Fritts & Alexander, 2003, and references therein). Studies have also shown that the solar terminator or the Moon's umbra projected onto the Earth during a solar eclipse can produce GWs (Altadill & Sole, 2001; Fritts & Luo, 1993; MacDougall & Jayachandran, 2011; Sauli et al., 2006).

GWs are often classified on the basis of their scales. Large-scale GWs propagate in the thermosphere and have horizontal velocities between 400 and 1,000 m/s, horizontal wavelengths greater than 1,000 km, and periods in the range of 30 min to 3 hr. Medium-scale GWs, which typically propagate in the lower atmosphere, have horizontal velocities between 100 and 250 m/s, wavelengths of several hundred kilometers, and periods between 15 and 60 min (Hocke & Schlegel, 1996; Hunsucker, 1982; Ogawa et al., 1987). GW amplitudes grow rapidly with increasing altitude because of the decreasing background density (Hines, 1960). In the thermosphere, GWs are further affected by dissipative processes including kinematic viscosity, thermal diffusivity, ion drag, wave-induced diffusion, and nonlinear wave interactions (Francis, 1973; Fritts & Alexander, 2003; Maeda, 1985; Richmond, 1978; Vadas & Fritts, 2005). Additionally, GWs moving against a background wind tend to propagate to higher altitudes because they are refracted by the background wind to a more vertical trajectory than those moving in the same direction (Fritts & Vadas, 2008).

GWs propagating in ionospheric regions interact with the ions through collisions and result in the neutrals driving ion transport along the magnetic field lines creating advection and compression of the plasma, traditionally called traveling ionospheric disturbances (TIDs; Hocke & Schlegel, 1996; Kirchengast et al., 1995). TIDs are broken into three different classes: large scale, medium scale, and small scale. Large-scale TIDs arise typically during geomagnetic storms accompanying large energy and momentum inputs in the auroral zones. These inputs result in strong heating, acceleration, and potentially very large amplitudes in the neutral and plasma density, temperature, and wind fields extending to high altitudes and readily propagate to equatorial latitudes (Hocke & Schlegel, 1996). Medium- and small-scale TIDs appear more frequently during geomagnetically quiet or moderately disturbed times and do not have a corresponding increase in occurrence frequency with increasing geomagnetic activity (Ogawa et al., 1987). At the medium and small scales TIDs have many sources. Some of these sources include the manifestations of GWs entering the thermosphere-ionosphere system from sources in the lower atmosphere (Hunsucker, 1982), the effects of Joule heating and Lorentz forces in the auroral electrojet, the presence of particle precipitation (Bertin, 1983; Richmond, 1978), and instabilities associated with *E* and *F* region coupling processes (Yokoyama et al., 2009).

To date, the modulation of high-latitude ionospheric transport by strong GWs has not been carefully studied. This study presents data from the Sondrestrom incoherent scatter radar (ISR) from 31 May 2003 that contains signatures of GW activity. These data were analyzed and have inspired an in-depth modeling study of the field-aligned transport in the *F* region and topside ionosphere in response to linear and nonlinear atmospheric GWs. This paper is organized with a presentation of the data used to guide modeling efforts in section 2, a description of coupled model system used for this study in section 3, followed by a discussion of the primary mechanisms driving ion upflow as discerned from the modeling activities in section 4, and finally summary and conclusions in section 5.

2. Data Motivating and Guiding Modeling Efforts

When TIDs are observed with ISR, such as Arecibo, PFISR/RISR, EISCAT, and Sondrestrom, there can be oscillations in all of the primary parameters, that is, electron density, electron temperature, ion temperature, and line-of-sight ion velocity (Bertin, 1983; David et al., 2018; Hocke et al., 1995; Kirchengast et al., 1995; Nicolls et al., 2004; Thome, 1964; Vlasov et al., 2011). Recent work has also shown that GW parameters may be derived from ISR measurements, provided sufficient spatial coverage is achieved (Nicolls & Heinselman, 2007; Nicolls et al., 2013; Vadas & Nicolls, 2007). From a study of 45 high-latitude TIDs, observed by the EISCAT radar at

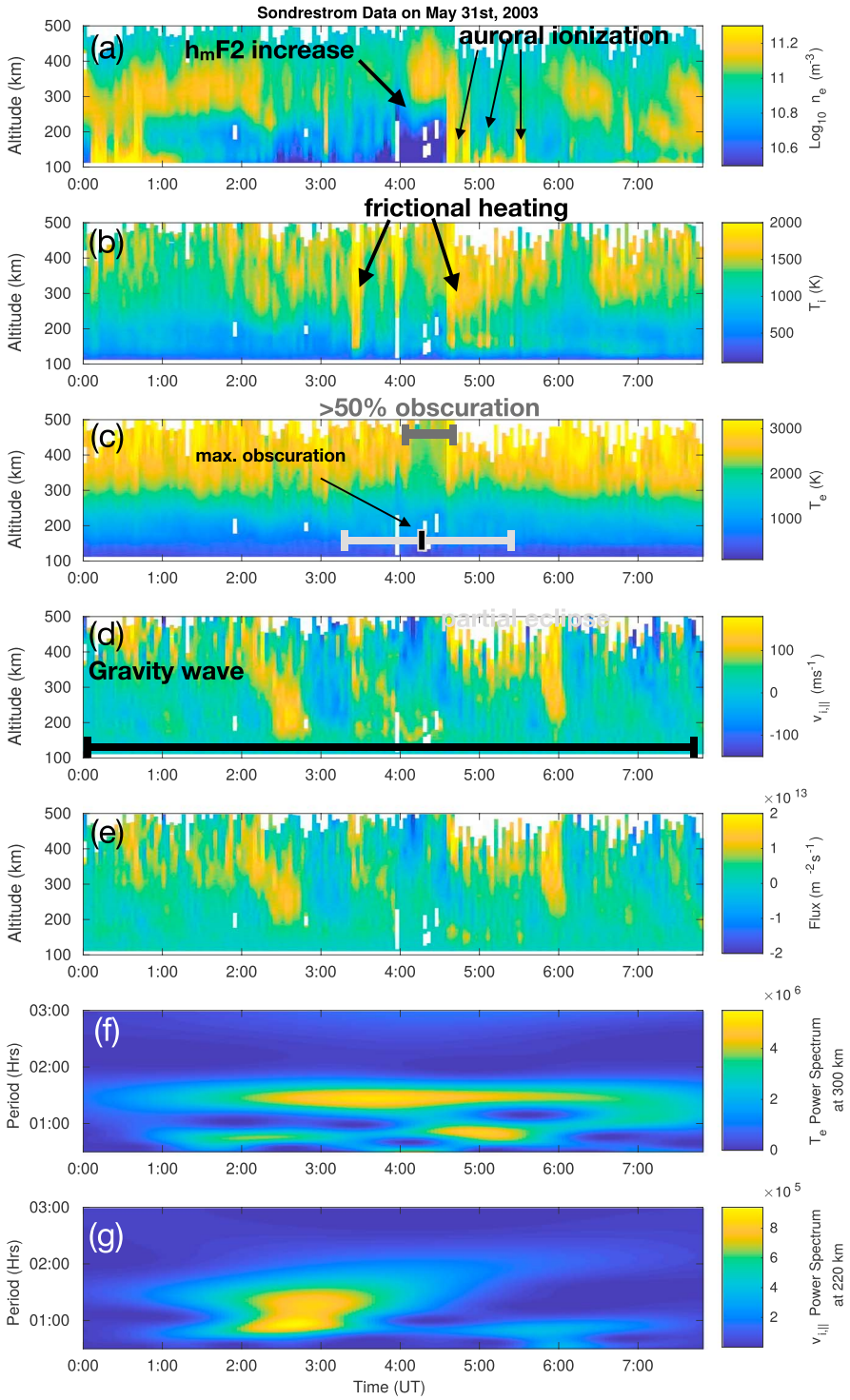

Figure 1. (a–e) The Sondrestrom incoherent scatter radar (ISR) data on 31 May 2003 and the corresponding Morelet wavelet analysis of the electron temperature at 300 km (f) and the line-of-sight velocity at 220 km (g), from 0:10 to 8:00 UT. The ~50 to 150 m/s alternating upward and downward ion flow (d) with a downward phase progression extends in some cases below hmF_2 over the course of this data set and suggests a GW influence.

Tromsø (Hocke et al., 1995), it has been suggested that the line-of-sight velocities are the best tracer for GWs since other ionospheric parameters can be easily disturbed by electron precipitation and frictional heating (Bertin, 1983).

On 31 May 2003 Sondrestrom's ISR observed line-of-sight velocity perturbations of ~50 to 150 m/s alternating upward and downward ion flow, extending in some cases below hmF_2, with a downward phase progression that suggests the presence of a GW (shown in Figure 1). Under normal ionospheric conditions it is fairly unusual to see upflow below hmF_2—to do so ostensibly requires neutral winds to overcome the effects of gravitational and pressure gradient forces (both downward). The radar, throughout this experiment, utilized a single look direction with an elevation of 80.5° which is well aligned with the local magnetic field lines. A time integration of 3 min and a height resolution of ~40 km were used. Regions in this data of large uncertainty, >90%, have been left white in lieu of error bars to indicate our confidence in the measurements.

Within the field of view for Sondrestrom, the GW perturbation appears, enhances, then diminishes in amplitude over ~7 hr (Figure 1d) and generates significant ionospheric flux (Figure 1e). The ISR data also show signatures of electron precipitation at 0:10–1:10 UT and 4:36–5:36 UT in the form of low-altitude (<200 km) electron density (Figure 1a) increases and high-altitude (>400 km) upflow in the line-of-sight velocity (Figure 1d). There are also instances of frictional heating, evident in the ion temperature (Figure 1b) from 3:24 to 3:30 UT and 4:36 to 4:42 UT. Neither of these energy inputs are spatially or temporally aligned with the line-of-sight velocity oscillations, indicating a GW/TID observation and not frictional heating-driven upflow (Type 1 of Wahlund et al., 1992) or electron heating-driven upflow (Type 2 of Wahlund et al., 1992).

There is also an annular eclipse that occurs within the observation window. At Sondrestrom, partial obscuration begins at 3:29 UT but local sunrise is at 4:00 UT. The full eclipse, where the disk of the moon is, visually, completely within the disk of the Sun begins at 4:23 UT and continues until 4:26 UT; a peak obscuration of 87.9% is achieved. The remaining partial eclipse ends at 5:20 UT. This eclipse event accounts for the decrease in *E* region density (Figure 1a) from 4:00 to 4:36 UT. There is also a ~500 K decrease in electron temperature (Figure 1c) at this time due to the reduction of EUV heating. The temperature decrease results in the lowering of the equilibrium scale height which drives the downward transport of ions, seen above the *F* region in the data at this time (Figure 1d), and potentially accounts for the rise in hmF_2 from 388 to 429 km and increase in *F* region density (Figure 1a) from 4:00 to 4:36 UT (Evans, 1965). *F* region dynamics are also subject to field-aligned and $E \times B$ transports. The elevated ion temperatures from 3:24 to 3:30 and 4:36 to 4:42 UT suggest the presence of significant $E \times B$ drift, and as a consequence the higher *F* region densities may have been convected into view from other latitudes and local times. At 4:36 electron precipitation, mentioned previously, occurs and obscures any remaining eclipse effects. The GW exists for several hours before, and after, the eclipse event and thus seems unlikely to originate from the eclipse.

A Morlet wavelet analysis is applied to the line-of-sight velocity oscillations, which has the clearest GW/TID signal in the data (see Figure 1f for the power spectrum at 220 km). The output is averaged at each altitude to get a single dominant period and then averaged again over all altitudes to provide the average period of the observed GW. One of the drawbacks of this averaging is that it results in the removal of any smaller scale, or higher frequency, variability in the data. Averaging across time and all available altitudes yields an estimated frequency of 78 min and vertical wavelength of 350 km for this GW event. The horizontal wavelength, according to the anelastic GW dispersion relation (cf. Fritts & Alexander, 2003), is 1,800 km. These estimated wave parameters have been used for our data-inspired modeling study of GW impacts on upflow in subsequent sections.

The wavelet analysis, when applied to the electron temperature at 300 km, also yields a GW/TID signal (Figure 1e) which is more difficult to see when looking at the electron temperature directly (Figure 1c). At this altitude there is a consistent dominant period of 88 min and subharmonics at a smaller average period of 44 min. The clear GW/TID signal in both the line-of-sight velocity, from ~0:30 to 4:00 UT, and electron temperature, from ~0:30 to 8:00 UT, illustrates an interconnected response in the ion parameters to the wave to be examined via numerical simulations in later sections. The eclipse impacts the GW/TID signature in the wavelet analysis of the line-of-sight velocity from ~4:00 UT onward and the electron temperature when the eclipse

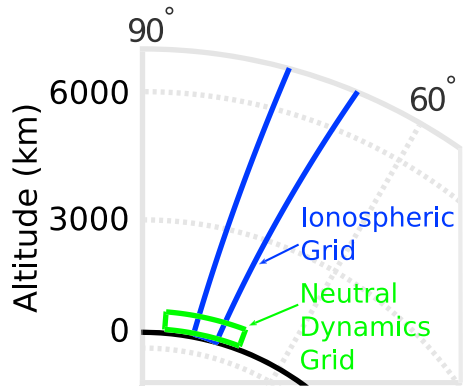

Figure 2. The ionospheric and atmospheric model grid alignment. The black line represents the surface of the Earth. The blue outline indicates the extent of the ionospheric model's grid (which extends up to 14,000 km above ground level and is well outside the range of this figure), and the green outline is for the atmospheric model. The overlap region between the blue area and the green area indicates where the models are coupled.

obscuration exceeds ~50%. The frictional heating and particle precipitation within the electron density and the ion temperature obscure the GW/TID signature in wavelet analysis of these parameters (which are not shown).

3. Modeling Approach

It is common to consider the ionosphere a passive tracer of the neutral gas with no feedback to the thermosphere (e.g., Clark et al., 1971; Davis, 1973; Hocke & Schlegel, 1996; Kirchengast et al., 1992; Testud & Francois, 1971). For this study we use the ionospheric model of Burleigh and Zettergren (2017) and the atmospheric model of Snively (2013) coupled via the approach discussed in Zettergren and Snively (2015, Appendix A). This allows for the GW perturbations from the neutral atmospheric model to drive the dynamical evolution (including upflow and outflow) in our ionospheric model.

The neutral dynamics model used in this study, informally referred to as Model for Acoustic-GW Interactions and Coupling, solves the conservative form of the Euler equations with the inclusion of the gravitational force and a Navier-Stokes description of viscosity. It is a variation of the model described by Snively and Pasko (2008), Snively (2013), and (Zettergren & Snively, 2015, Appendix A). It solves the Euler equations in conservative form using a finite volume method based on LeVeque's *f wave* approach (LeVeque, 1997, 2002), with the inclusion of gravity via the method described in Bale et al. (2003).

The ionospheric model used in this study and described in detail in Burleigh and Zettergren (2017) (GEMINI-TIA) is an anisotropic extension of the model originally developed in Zettergren and Semeter (2012) and expanded in Zettergren and Snively (2013), Zettergren et al. (2014), and Zettergren and Snively (2015). This fluid model solves the 2-D nonlinear equations for the conservation of mass, momentum, parallel energy, and perpendicular energy for each species s relevant to the E and F regions and topside ionosphere ($s = O^+$, NO^+, N_2^+ O_2^+, N^+, and H^+) and is coupled to a quasi-static treatment of auroral and neutral dynamo electric currents.

Perturbations from the atmospheric background state are passed from the neutral dynamics model into the ionospheric model in a one-way coupling. Presently NRLMSISE-00 (Picone et al., 2002) is used to define background conditions in both models though user-specified profiles may be used as well. Perturbations communicated between the models include variations in neutral species density (specifically O, N_2, and O_2 for this study), velocity, and temperature. The passing of these coordinated disturbances incorporates influences of the simulated GW from the neutral atmospheric model into the ionospheric model through ion-neutral collisions/reactions and dynamo source terms in the electrodynamic equations solved by GEMINI-TIA. Neutral variations are communicated between the models every minute and interpolated to the current time step. In addition, there is also a spatial interpolation and rotation step to convert from the neutral dynamics model's Cartesian grid to the ionospheric model's tilted dipole grid.

Figure 2 shows the grids used by the two models for the simulations presented in this study. The blue outline indicates the extent of the ionospheric grid, and the green outline shows the atmospheric grid (the black line represents the surface of the Earth). The overlap region between the blue and green areas is where the neutral dynamics are coupled into the ionospheric model. The atmospheric model uses a uniform mesh that has horizontal grid spacing (x direction) of 5 km and a vertical grid spacing (z direction) of 1 km with an upper boundary of 500 km and a lower boundary of 88 km. The width is large enough to contain one wavelength, 1,800 km for this study. The ionospheric grid uses a tilted dipole configuration (Huba et al., 2000) and has variable spacing currently set to ~6–8 km in the E and F regions, with increasing grid size toward higher altitudes, and a top boundary altitude of ~14,000 km. The upper reaches of the ionospheric grid (>2,500 km) act as a buffer region to avoid boundary effects from impacting the solutions (Burleigh & Zettergren, 2017). The model's geographic location for the simulations presented in this paper has been centered on Sondrestrom, 66.99°N and 309.05°E, where the ISR data motivating this study was recorded.

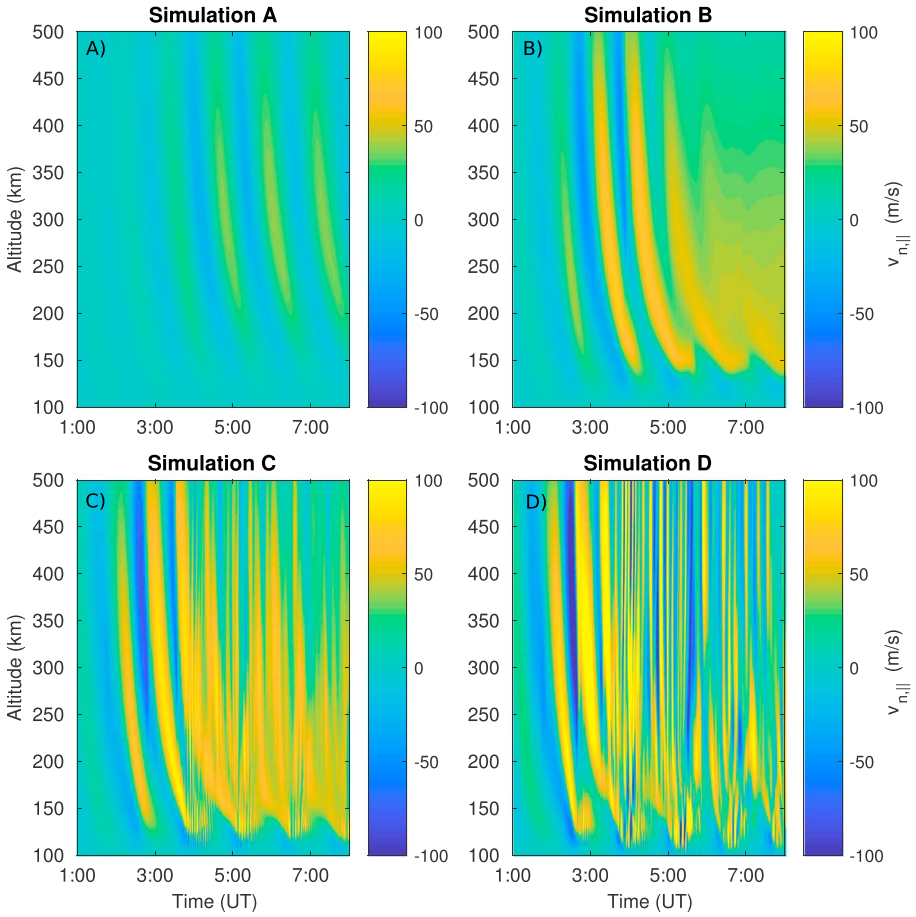

Figure 3. The field-aligned velocity component of the gravity waves generated by the neutral dynamics model after rotating into the ionospheric model's tilted dipole grid structure. (A–D) In all four simulations, A, B, C, and D, the gravity wave is excited by vertical body forcing with a period of 78 min. The strength of the wave is ramped up slowly over 117 min to avoid start-up wave breaking and acoustic waves and then held steady until the end of the simulation.

4. Ionospheric Response to GW Forcing

Four simulations are presented here to illustrate the ion field-aligned transport response to different strengths of large-scale atmospheric GWs. The initial conditions of the ionospheric model for each simulation have been tuned to resemble the background level densities observed via ISR (section 2). Since we do not have detailed knowledge of the source location, strength, propagation direction, and excitation mechanism, the GW is excited in the neutral atmosphere model by vertical body forcing chosen to approximately describe the spectrum of the observed ionospheric responses. The forcing function is given by

$$F_z(x,z,t<t_c) = A\ n_n\ \exp\left(-\frac{(z-z_c)^2}{2\sigma_z^2}\right)\exp\left(-\frac{(t-t_c)^2}{2\sigma_t^2}\right)\cos\left(\frac{2\pi}{\tau}(t-t_c)-\frac{2\pi}{\lambda_x}x\right) \quad (1)$$

where A is the peak acceleration of the vertical wind, set to 0.4, 2, 4, and 7 m/s^2 for the four simulations (labeled A, B, C, and D, respectively), which gets multiplied by the local neutral mass density (ρ_n) to produce the forcing amplitude. In equation (1) a forcing altitude (z_c) of 110 km and a half-width (σ_z) of 10 km are chosen. The Gaussian envelope's half-width is chosen to generate a localized wave forcing in the lower thermosphere, to produce a quasi-monocromatic spectrum of upward propagating waves rather than a single mode. The period of the GW source (τ) in all four simulations is 78 min with a horizontal wavelength λ_x of 1,800 km and a vertical wavelength of ~350 km. Note that the vertical wavelength of the simulated GW does not remain constant with altitude due to temperature variations. The GW source in all of the simulations is ramped up slowly over 117 min (σ_t) to avoid transient wave breaking and acoustic waves. When the GW reaches full strength ($t \geq t_c$), the forcing takes the form of

$$F_z(x,z,t \geq t_c) = A\ n_n\ \exp\left(-\frac{(z-z_c)^2}{2\sigma_z^2}\right)\cos\left(\frac{2\pi}{\tau}(t-t_c)-\frac{2\pi}{\lambda_x}x\right) \quad (2)$$

until the end of the simulation (Heale et al., 2014). All of the simulations run from 0:00 to 8:00 UT.

The field-aligned velocity component of the GWs generated by the neutral dynamics model and interpolated onto the ionospheric grid is presented in Figure 3. The four simulations presented here differ as they depend critically on the GW strength. For Simulation A (Figure 3A—corresponding to the smallest amplitude wave) the GW is very regular in motion and once the GW has been ramped up to full strength there is a maximum neutral upflow (downflow) of 38 m/s (−28 m/s). This GW does not break, and there are minimal nonlinear wave effects (e.g., energy deposition into other wave modes). For Simulation B (Figure 3B), there is significant momentum deposition into the mean flow but minimal wave breaking. This combination of effects is responsible for the increase in the mean flow, from 4:30 UT onward to the end of the simulation, converting the wave upflow/downflow pattern to a weaker, yet net, upflow. If the GW were to be traveling in the opposite direction, this momentum deposition would result in a decrease in the mean flow and larger downflows. The GW still generates a maximum upflow (downflow) of 76 m/s (−52 m/s) before the nonlinear wave effects dominate the dynamics. For Simulation C there is an increase not only in the mean flow, from 4:00 UT onward to the end of the simulation, but also in small-scale, intense, upflow/downflow generated from wave breaking effects below ~200 km. This GW generates an upflow (downflow) of 100 m/s (−77 m/s) before the breaking occurs, and a maximum of 195 m/s (−87 m/s) is reached within a region of wave breaking. For Simulation D (Figure 3D), there is only modest momentum deposition into the mean flow but significant wave breaking. More energy is deposited into small-scale wave modes generated by wave breaking and less into the mean flow than that seen in Simulations B and C. An upflow (downflow) of 108 m/s (−122 m/s) before the breaking occurs, and a maximum of 339 m/s (−291 m/s) is reached within a region of wave breaking and is generated by this GW in Simulation D.

As the GW dynamics evolve over time, the neutral atmosphere perturbations act upon the ionosphere and drive ion upflow/downflow (see Figure 4). Nonlinear wave effects and wave breaking play an important role in modifying the ion response in each simulation. The total ion density (Figures 4-1A–4-1D) is modulated by the GW motions, through ion-neutral drag. It should be noted that the general increase in ion density over the latter half of each simulation is due, in part, to photoionization from a changing solar zenith angle. It is summer so the regions >110 km are still illuminated by the Sun. This has a tendency to reinforce the ion response to neutral forcing as the day progresses.

The smallest amplitude GW, Simulation A (Figure 4-1A), drives density perturbations that are very regular with a clear wave-like structure. The increase in mean flow, within the driving GW for Simulations B and C, results in more transport and a larger density (Figures 4-1B and 4-1C). These densities reach 1.0×10^{11} and 1.1×10^{11} m^{-3} at an altitude of 500 km, respectively, by the end of the simulation. This is much larger than the corresponding values of 7.5×10^{10} or 8.8×10^{10} m^{-3} in Simulations A and D, respectively. Simulation D contains a large amount of wave breaking, which passes energy into smaller-scale wave modes resulting in very irregular but strong, density perturbations (Figure 4-1D). The ion-neutral drag in this case is strong enough to lift the *F* region peak to higher altitudes; see ~4:15 UT in Figure 4-1D where this effect is the greatest.

In addition to the ion density perturbations, there is also strong coupling between the atmospheric temperature and the ion temperature from the bottom of the simulation up through the *F* region peak. The average ion temperature (defined as $1/3T_{||} + 2/3T_{\perp}$) of O^+ from each of the simulations is presented in Figures 4-2A–4-2D. The GW dynamics passed between models included temperature perturbations which drive the ion-neutral thermal coupling (via heat exchange) within the model coupled region.

The ion upflow driven in Simulation A, like the modulating GW, is very regular. At 1,000 km, it reaches a maximum upflow of 80 m/s at 6:12 UT. Driving with a larger amplitude GW which contains significant momentum transfer into the mean flow, such as that in Simulation B, generates persistent upflow, on average 54 m/s, from 4:00 UT onward for altitudes above the *F* region peak (Figure 4-3B). Prior to that, a maximum upflow of 108 m/s at 1,000 km at 3:30 UT was reached. The mean flow increase effect is also present in Simulation C. Coupled with wave breaking, it transports more ions to higher altitudes, results in a smaller average field-aligned velocity, 48 m/s from 4:00 UT onward at 1,000 km, than the maximum upflow of 127 m/s reached at 3:18 UT, and produces a larger ion particle flux (see Figure 4-4C here and Figure 9 for more details). The wave breaking

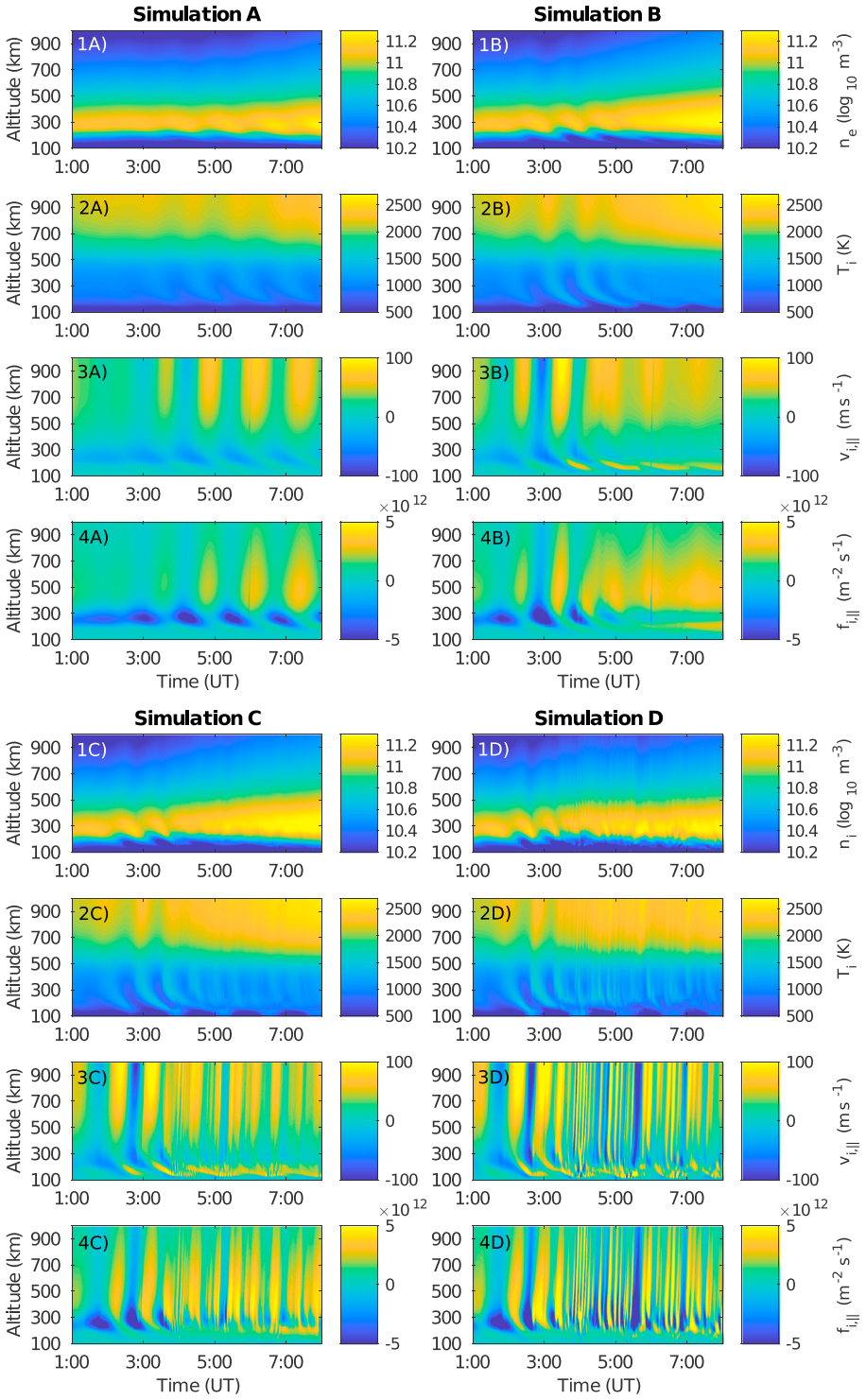

Figure 4. The ion dynamics from the center field line of the model grid from 1:00 to 8:00 UT, for Simulations A, B, C, and D (each column of plots corresponds to a simulation in alphabetical order) for, in descending order, the total ion density (1A–1D), O^+ absolute temperature (2A–2D) where the parallel and perpendicular temperatures have been averaged as $1/3T_{||} + 2/3T_{\perp}$, the O^+ field-aligned velocity (3A–3D), and the ion flux (4A-4D)

effects are also present in Simulation D and dominate the GW-driven dynamics resulting in fine-scale, intense upflow/downflow. At 1,000 km the O^+ field-aligned velocities maximize at 134 m/s at 3:00 UT before the GW breaks and reaches in excess of 240 m/s after breaking.

The ion flux, generated by the modulating GW, maximizes in the *F* region where densities are still large. Comparing the four simulations at 500 km, Simulation A generates a maximum flux of 2.9×10^{12} m^{-2} s^{-1} at 7:27 UT (Figure 4-4A), Simulation B generates a maximum flux of 3.2×10^{12} m^{-2} s^{-1} at 7:20 UT (Figure 4-4B), Simulation C generates a maximum flux of 5.3×10^{12} m^{-2} s^{-1} at 5:31 UT (Figure 4-4C), and Simulation D generates a maximum flux of 1.7×10^{13} m^{-2} s^{-1} at 4:06 UT (Figure 4-4D). Within Simulation D, the effects of wave breaking also generate a strong downward flux of -1.1×10^{13} m^{-2} s^{-1} at 5:36 UT at this altitude. The simulations that contain significant wave breaking, Simulations C and D, generate large fluxes several hours sooner than Simulations A and B. Wahlund and Opgenoorth (1989) suggest that a minimum threshold of 10^{13} m^{-2} s^{-1} is needed for an ion flux to have the potential to become outflow. Only Simulation D exceeds this threshold, but with just the GW driving ion motions escape speed is not reached. All of the simulations contain transport that is enough to alter the ion populations available for other energization processes at this altitude, such as frictional heating, auroral precipitation, or transverse wave heating.

Because the ISR velocity data were analyzed for wave parameters and used to inspire the coupled model study, this is the primary parameter used to compare the model outputs back to the ISR data. Velocity was chosen for the comparison as it is most closely mirrors the effects of the GWs, whereas electron temperature is directly altered by auroral precipitation and ion temperature is controlled to a large degree at high latitudes by frictional heating from strong E × B drifts. Lastly, density is extremely complicated because it is affected by precipitation, heating (which alters chemistry), and convection of density gradients. Of the four simulations presented here, the ionospheric response to the GW in Simulation C most closely resembles the data from the May 2003 GW presented in Figure 1. The field-aligned velocity has a similar dynamic range when compared to the data, viz. ∼50–150 m/s. Although Simulation C contains moderate wave breaking, evidence of wave breaking, if present in the data, is difficult to ascertain due to the long integration time of the ISR data.

The O^+ velocity period that contains the most power at every altitude and time step is plotted in Figure 5 using a Morelet wavelet analysis (Torrence & Compo, 1998) of the field-aligned O^+ velocity. This highlights the ion response to the four wave situations used in this study and where the nonlinear GW effects have the greatest impact. All of the simulations contain, at the lowest altitudes, a primary ion velocity period that matches the GW forcing period of 1.3 hr. In Simulation A, there is a coherent ion response to the GW (evidenced by the relatively stable, in altitude and time, periodicities) that contains minimal nonlinear effects, including wave breaking (Figure 5A). Self-acceleration (Fritts et al., 2015) leading to shear that destabilizes the GW in Simulations B and C, from 200 to 500 km, drives the ion velocity period to shorter periods from 2 to 6 UT (Figure 5B and Figure 5C, respectively). In Simulation C (Figure 5C) the locations of dark blue in this panel, where the dominant velocity period is 5 min or less, indicate the presence of moderate wave breaking and occur most readily at altitudes below 250 km, where viscous effects are not too strong. Times of strong wave breaking dominate the wave power and resulting ion response (Figure 5D) in Simulation D throughout all altitudes as indicated by many abrupt transitions to very short periods in Figure 5D.

Ion motions are driven by GWs through a series of interconnected processes and may result in upflow above the *F* region peak. This is illustrated in Figure 6, which has background conditions from a control simulation subtracted from the simulation results to isolate the GW-driven responses. This background subtraction also has the added benefit of removing the effects of changing solar zenith angle on photoionization rates. From GW-driven ion-neutral drag, electron density modulations (Figures 6-1A–6-1D) alter the electron temperature (Figures 6-2A–6-2D) largely by controlling the relative amounts of photoionization heating and collisional cooling. In general, at low altitudes (<250 km) the electron temperature modulation is due to density perturbations. At higher altitudes (>250 km) electron temperature variations are due to the quick transport of heat (i.e., thermal conduction) along the field lines. These higher-altitude electron temperature variations then modulate the ambipolar electric field driving ionospheric upflow and downflow (Figures 6-3A–6-3D) above the regions directly modified by the GW.

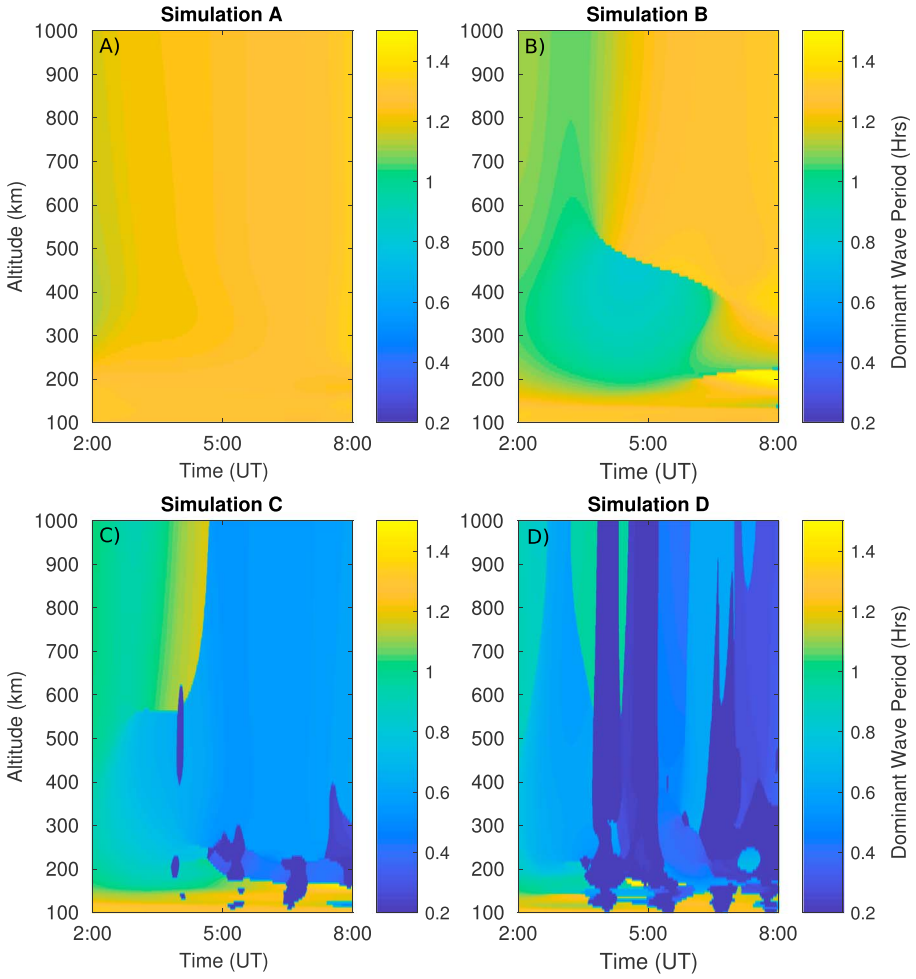

Figure 5. The results of a Morelet wavelet analysis on the field-aligned O^+ velocity and selecting the period that contains the most power at every altitude and time step illustrates the transition between a simple gravity wave/traveling ionospheric disturbances with minimal nonlinear effects and no-wave breaking (A), to situations where there is predominantly momentum transference (B), to a combination of momentum deposition and wave breaking (C), to the other extreme where there is primarily wave breaking (D).

Ion densities are controlled by the interplay between the production, loss, and inflow transport processes that are described by the continuity equation

$$\frac{\partial \rho_s}{\partial t} = \underbrace{-\nabla \cdot (\rho_s \mathbf{v}_s)}_{\text{Inflow}} + \underbrace{m_s P_s}_{\text{Production}} \underbrace{-L_s \rho_s}_{\text{Loss}} \tag{3}$$

where ρ_s is the ion mass density, $\mathbf{v}_s$ is the velocity, and m_s is the ion mass for species s. P_s is the species volumetric production rate ($m^{-3}\ s^{-1}$) and includes ion creation from chemical production, photoionization, and impact ionization, while L_s is a loss frequency term (s^{-1}) encompassing chemical loss processes. Inflow transport is influenced by the ion-neutral drag motions.

The inflow transport, production, and loss terms from equation (3) for O^+ are each integrated over 200–225 km altitudes (Figure 7b) and 300–325 km (Figure 7a) and across the horizontal span of the ionospheric grid. Hence, we are able to decompose the relative effects of transport versus chemical loss versus production variation in producing the GW-driven plasma density fluctuations that dominate the ionospheric response in these two distinct altitude regions. In this analysis the results from the control simulation have been subtracted to isolate wave-driven parts of the responses.

In the lower attitudinal region (Figure 7b), for Simulations B (red dash line) and C (red dash-dotted line), the GW motions have generated significant upflow, which results in outflow from this region (characterized by

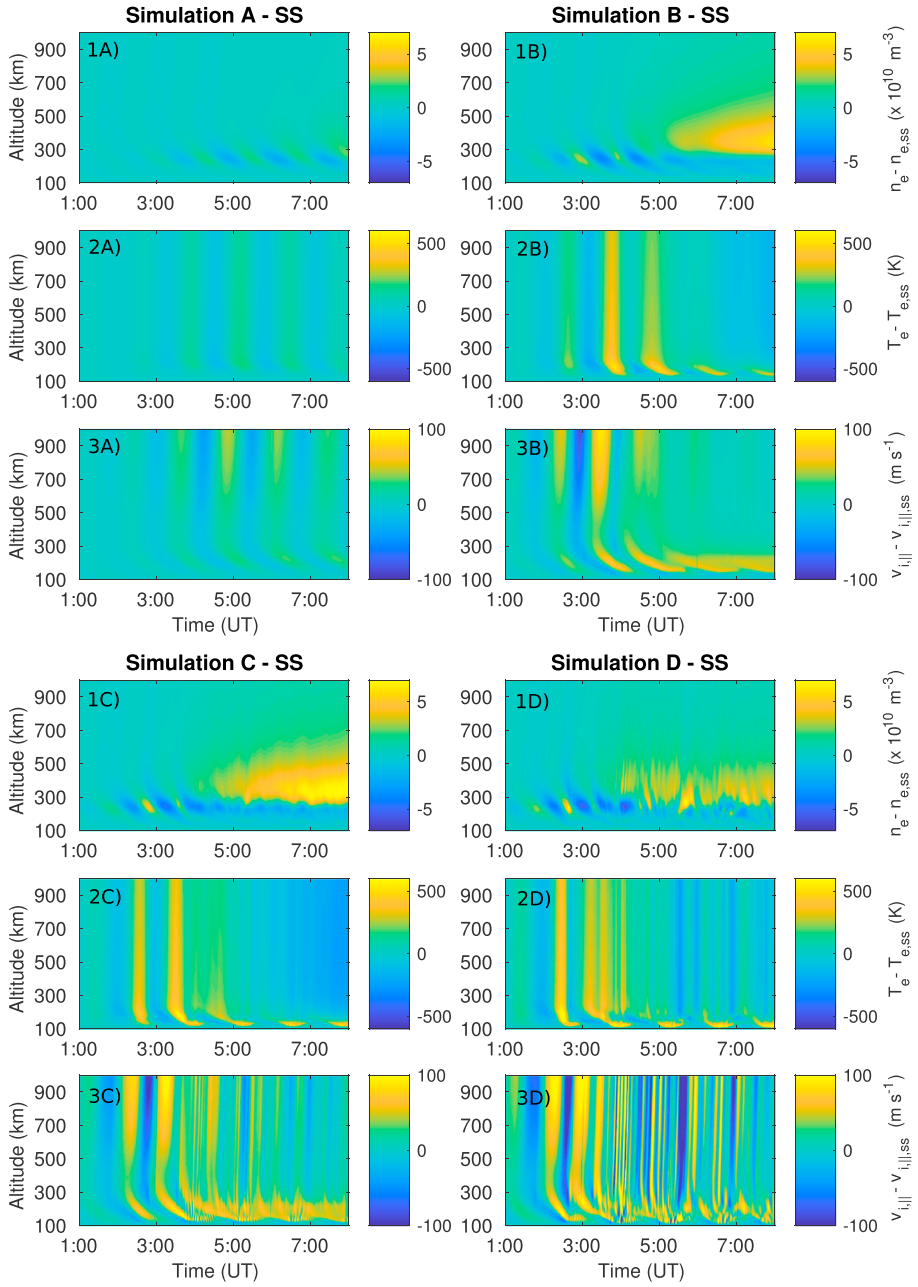

Figure 6. A no-GW, control simulation has been subtracted from the four simulations, A, B, C, and D, to isolate the gravity wave-driven effects. The electron density difference, electron temperature difference, and the field-aligned ion velocity difference for each simulation are presented in descending order.

negative inflow). This depletes the local density and reduces chemistry loss processes for Simulations B (blue dash line) and C (blue dash-dotted line). Simulation A, corresponding to a linear GW, contains quite idealistic perturbations in both inflow transport (Figure 7b, red solid line) and loss (Figure 7b, blue solid line).

At higher altitudes, 300–325 km (Figure 7a), GW motions drive an increase in inflow transport from 4:00 UT onward through the end of the simulation, for Simulations B (red dash line) and C (red dash-dotted line). This increases the local density, and the rate of chemistry loss processes in response to the increase in density, for both Simulations B (blue dash line) and C (blue dash-dotted line). This behavior is opposite from what was observed in the 200- to 225-km altitude range (Figure 7b). The GW increase in mean flow from ~4:00 UT onward is directly responsible for the O^+ density increases seen within Simulations B and C, and the lack of

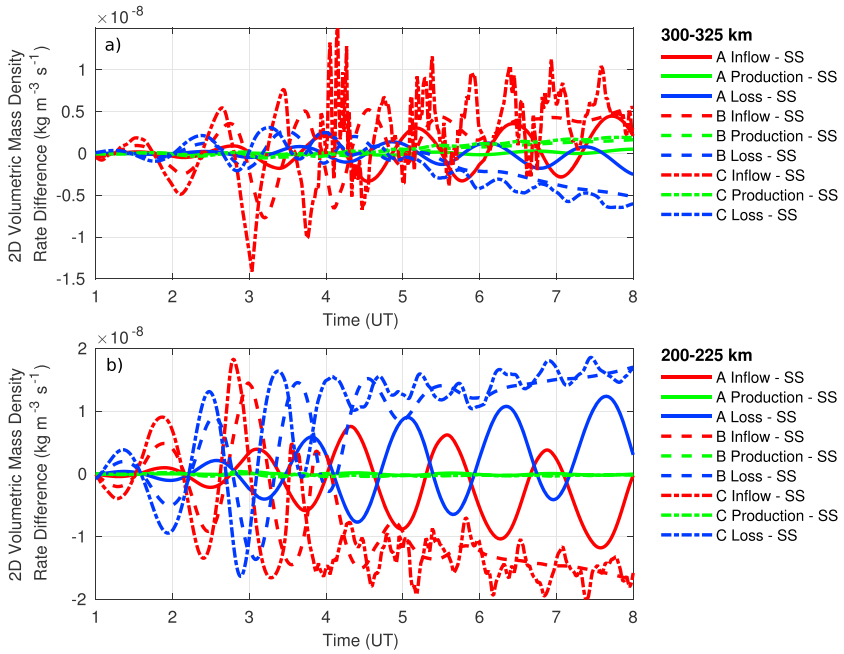

Figure 7. A comparison of the production, loss, and inflow transport terms, for O^+, integrated over 25-km altitude ranges from 300 to 325 km (a) and 200–225 km (b) across the span of the model grid to encompass latitudinal differences. The result from the no-GW control simulation (SS) has been subtracted to isolate the GW driven changes. Simulation D has been left out of this figure due to the excessive breaking rendering it illegible.

a similar density increase in Simulation D which contains more wave breaking and Simulation A which is not strong enough to generate this effect (see Figures 6-1A–6-1D).

As the GW modulates the neutral and ion densities, the electron collisional cooling (Figures 8-1A–8-1D, for Simulations A–D, respectively) and the photoionization heating rates (Figures 8-2A–8-2D) are also directly altered. Background conditions from a control simulation have been subtracted from the simulations in Figure 8 to isolate the GW impacts. These effects are strongest at altitudes between 150 and 200 km where the neutral atmosphere density perturbations have the greatest impact. Density increases at *F* region altitudes give the plasma a larger effective heat capacity yielding a smaller temperature response to the fixed photoionization input (manifesting as cooler electron temperatures in the latter portion of Simulations B and C). These periods of reduced/increased heating quickly conduct up the magnetic field lines and contribute significantly to the electron temperature variations in the topside ionosphere.

The total effect of the combined photoionization heating rate and electron collisions cooling rate (Figures 8-3A–8-3D) drives the electron temperature response. The total effect ranges from −5 to 9 K/s in Simulation A with the minimum and maximum occurring at 6:50 and 7:10 UT, respectively, at 230 km. The GW modulating this simulation continues undisturbed over time due to the lack of wave breaking and nonlinear effects. From Simulations B the heating difference ranges from −26 to 34 K/s with the minimum and maximum occurring at 4:12 and 3:45 UT, respectively, at 156 km. The minimum occurs half a wave period after the maximum and before the momentum transfer alters the wave dynamics (see Figure 5 for discussion). In Simulations C the heating difference ranges from −56 to 45 K/s with the minimum and maximum occurring at 3:46 and 3:33 UT, respectively, at 156 km. The time shift between Simulations B and C in reaching the minimum and maximum heating rate differences is due to the self-acceleration generated by the wave dynamics which alter the period of the wave. Wave breaking effects do create brief periods of comparable heating, especially near the GW forcing region in Simulation C. In Figure 8-3C, the total heating effect of Simulation C, centered around 300 km from 5:00 UT onward, has net cooling which is responsible for the cooling of electron temperature (Figure 6-3C) in response to the increase in density (Figure 6-2C) driven by the mean flow increase within the GW (Figure 6-1C). The strongest upflow of this simulation occurs just before wave breaking which is when the maximum heating occurs as well. The heating difference ranges from −44 to 51 K/s in Simulation D with the minimum and maximum, not considering lower altitude wave breaking effects, occurring at 2:36

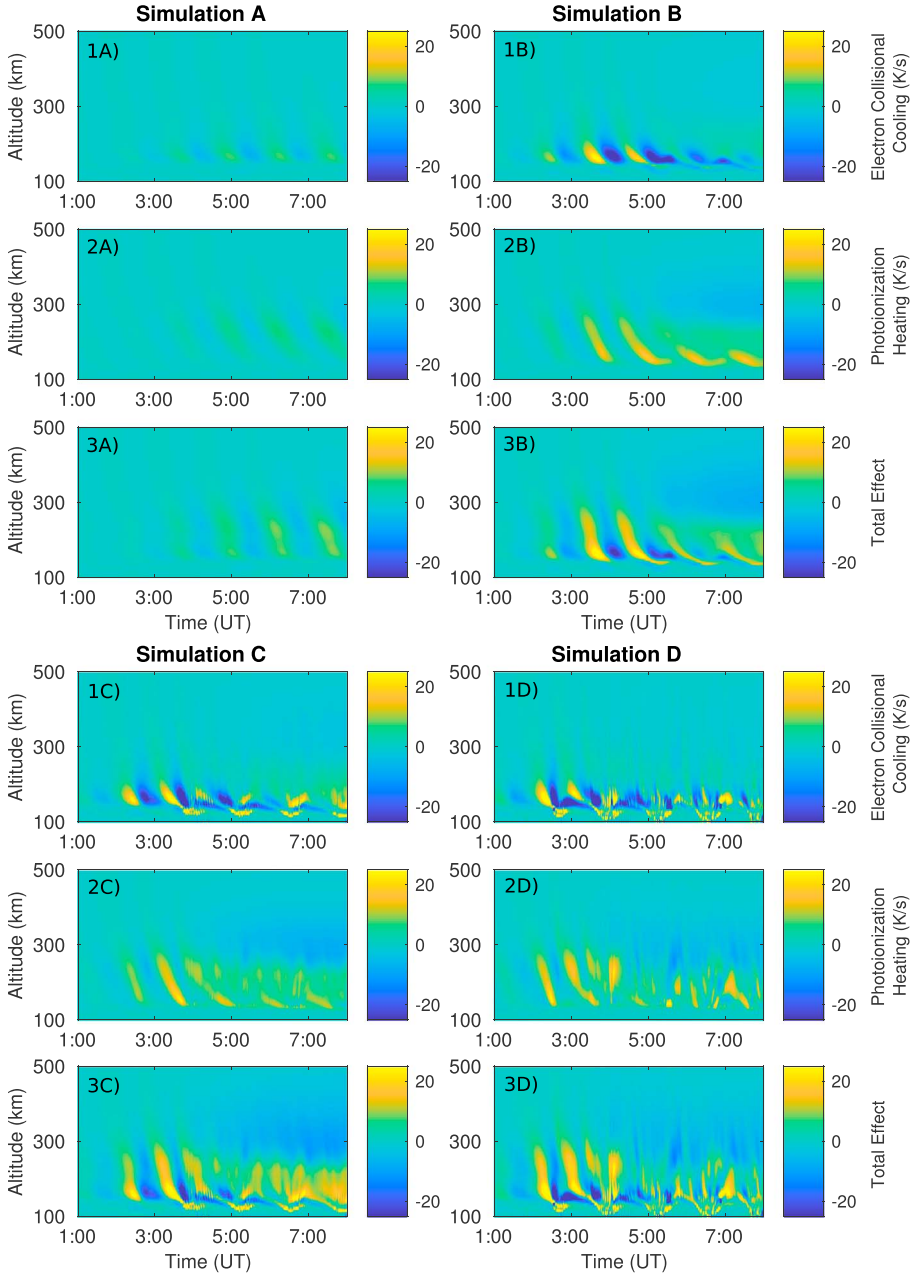

Figure 8. The gravity wave (GW)-modulated electron cooling rate due to ionospheric and atmospheric collisions/interactions (1A–1D), the GW-modulated photoionization heating rate (2A–2D), and the total effect of these two processes (3A–3D) have the background conditions from a control simulation subtracted off to isolate the GW effects.

and 2:26 UT, respectively, at 156 km. The time separation between the minimum and maximum total heating effects is less than half of a wave period because of the onset of wave breaking. The wave breaking in this simulation also drives periods of short, ~5 min or less, intense heating near or within the forcing region (e.g., 200 K/s at 3:54 UT at 110 km).

Increases in electron temperature rapidly conduct up the field lines, heating and expanding the local population at higher altitudes; the ambipolar electric field drives an ion response well outside the region where direct, ion-neutral coupling is significant. The O^+ flux at 1,000 km, shown in Figure 9a, reaches a maximum of 1.3×10^{12} m^{-2} s^{-1} at 7:32 UT in Simulation A, 1.5×10^{12} m^{-2} s^{-1} at 3:33 UT in Simulation B, 1.9×10^{12} m^{-2} s^{-1} at 6:43 UT in Simulation C, and 5.2×10^{12} m^{-2} s^{-1} at 4:10 UT in Simulation D. The wave breaking in Simulation D

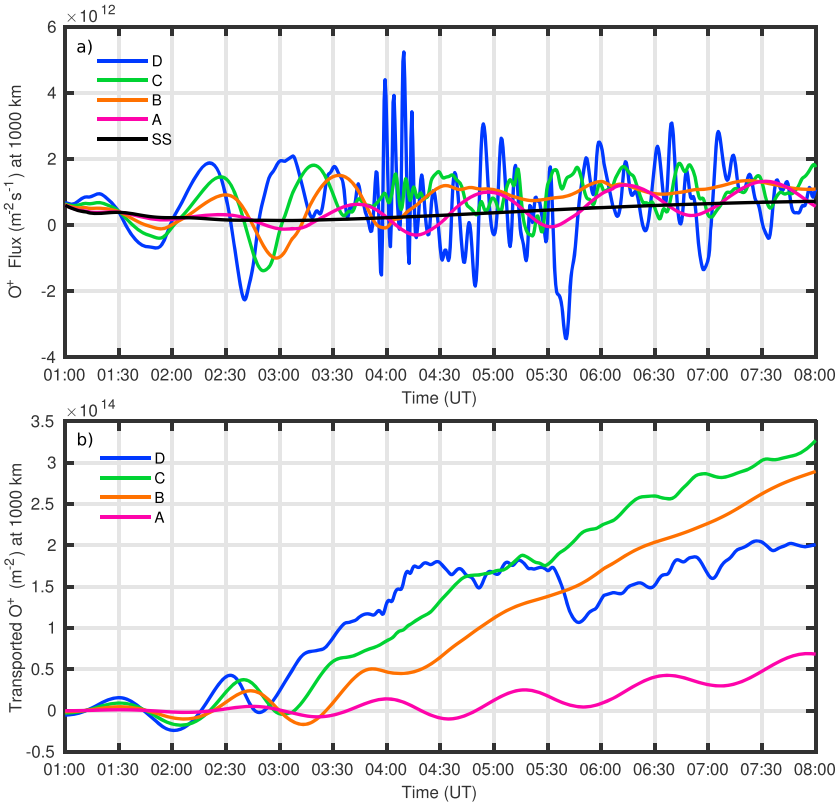

Figure 9. The (a) O^+ flux from Simulations A–D at 1,000 km and (b) total number of O^+ particles transported through this location on the center field line of the ionospheric model grid from 1:00 to 8:00 UT. The control simulation, labeled with SS, has been included (black line) for comparison in Figure 9a. The control simulation transported O^+ has been subtracted from the transported O^+ in Simulations A–D (Figure 9b) to highlight gravity wave-driven effects.

around 4:00 UT drives the largest O^+ flux (Figure 9a) and also limits the total O^+ transported upward through this location (Figure 9b).

Integrating the O^+ flux in Figure 9a calculates the total number of particles passing, per square meter, through the center field line of the ionospheric model grid at 1,000 km and is one way of quantifying of the effectiveness of the GW to generate ion upflow. The control simulation transported O^+ has been subtracted from the transported O^+ in Simulations A–D (Figure 9b) to highlight GW-driven effects. By the end of Simulation A the total number of particles transported was 5.0×10^{14} particles/m^2, Simulation B had 7.2×10^{14} particles/m^2, Simulation C had 7.6×10^{14} particles/m^2, Simulation D had 6.3×10^{14} particles/m^2, and the control simulation had 4.3×10^{14} particles/m^2. The relative coherence of the GW also affects the transport efficiency. When the GW contains excessive breaking, the pulses of upflow and downflow are large but combined have a smaller net response than a smaller but more consistent upflow, that is, excessive breaking in Simulation D versus weaker but more consistent upflow in Simulation C (or B).

This topside transport is enough to alter the ion populations available for secondary acceleration processes, such as transverse wave heating, that can lead to outflow into the magnetosphere. Wave heating has been added at 7:30 UT for 5 min to the GWs driving Simulations C and D, in two additional simulations denoted Simulation C_W and Simulation D_W (see Figure 10, dashed lines evident from 7:30 onward). In a third new simulation, denoted by SS_W, the control simulation also has wave heating applied at the same UT for additional comparison. The wave heating is accomplished through the use of the resonant heating term, $\dot{W}_{s,\perp}$, included in the perpendicular energy equation within the model that encompasses the acceleration of ions by transverse plasma waves (Burleigh & Zettergren, 2017). This gyroresonant (cyclotron) energy transfer is the most efficient in regions of low ion-neutral collision rates and is therefore not very effective below 500 km except in extreme cases (e.g., Whalen et al., 1978). The present form of the model (Burleigh & Zettergren, 2017) uses an empirical specification of this heating term:

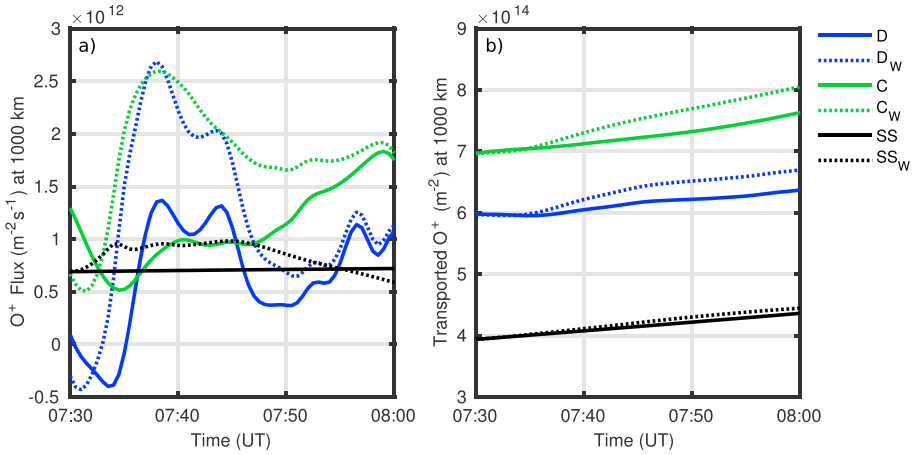

Figure 10. The gravity wave-driven topside transport is enough to alter the ion populations available for secondary acceleration processes, such as transverse wave heating, that can lead to outflow into the magnetosphere. Transverse wave heating has been added at 7:30 UT, for a duration of 5 min, to the gravity waves driving Simulations C and D and the no-wave control simulation. (a) O^+ flux and (b) total number of O^+ particles transported along the center field line of the model grid at 1,000 km. In these panels the dashed lines are the new simulations that contain 5 min of transverse wave heating.

$$\dot{W}_{s,\perp}(\omega) = 2m_s n_s \left(\frac{\eta q_s^2}{4m_s^2}\right) |E_o|^2 \left(\frac{\omega}{\omega_o}\right)^{-\alpha} \tag{4}$$

where ω is the local gyrofrequency for each ion, η is the fraction of the wavefield which is left-hand polarized, assumed to be 0.125 (Chang et al., 1986), α is the spectral power index, assumed to be 1.7 (Crew et al., 1990), and $|E_o|^2$ is the wave power spectral density set here to be 0.3 $(mV/m)^2/Hz$ with the reference frequency ω_o assumed to be 6.5 Hz (Retterer et al., 1983; Zeng & Horwitz, 2008; Zeng et al., 2006). This type of heating occurs primarily in collisionless regions; the resulting ion distributions remain highly anisotropic and are accelerated by the mirror force, attaining large field-aligned velocities high above the heating region.

The applied transverse wave heating (Figure 10) results in the O^+ flux to a peak effect 8 min after onset (Figure 10a); note that the wave heating was only applied from 7:30 to 7:35 UT. The total number of particles transported through 1,000 km on the center field line of the model grid is shown in Figure 10b. The addition of transverse wave heating raises the flux at 7:38 UT from 8.5×10^{11} in Simulation C (green solid line) to 2.6×10^{12} m^{-2} s^{-1} in Simulation C_W (green dashed line) and from 1.3×10^{12} in Simulation D (blue solid line) to 2.7×10^{12} m^{-2} s^{-1} in Simulation D_W (blue dashed line). This is a percent increase of 206% and 107%, respectively. For further comparison the wave heating has also been applied to the no-wave control simulation (black solid line) and only raises the O^+ flux from 7.0×10^{11} in Simulation SS to 9.5×10^{11} m^{-2} s^{-1} in Simulation SS_W (black dashed line) at 7:38 UT. This is a much smaller percent increase of only 35%. Ionospheric modulation by thermospheric GWs can significantly drive ion upflow and impact the ion populations available for outflow to the magnetosphere.

5. Conclusions and Future Work

Four simulations have been presented here to show how the high-latitude ionosphere can be modified by the presence of large-scale GWs, with particular focus on ionospheric plasma transport throughout the *F* region and topside. Neutral velocity perturbations modulate the ion density as the GW forcing progresses over time. These ion density modulations alter the electron collisional cooling rate as well as the photoionization heating rate. Combined, the net effect of these density-dependent processes results in periods of elevated or decreased electron temperatures. These temperature variations conduct up geomagnetic field lines altering plasma populations at altitudes well above the GW coupling region and through the ambipolar electric field drive an ion response as well. The result of this chain of processes is an ion upflow/downflow response at higher altitudes, altering the populations available for secondary acceleration processes that lead to outflow into the magnetosphere.

Along the center field line of the simulation at 1,000 km, the O^+ flux reaches a maximum of 1.3×10^{12} m^{-2} s^{-1} at 7:32 UT in Simulation A, 1.5×10^{12} m^{-2} s^{-1} at 3:33 UT in Simulation B, 1.9×10^{12} m^{-2} s^{-1} at 6:43 UT in Simulation C, and 5.2×10^{12} m^{-2} s^{-1} at 4:10 UT in Simulation D at 1,000 km. The maximum upflow often occurs just before wave breaking which causes wave power to be transferred to smaller-scale wave modes and out of the primary wave, except in the case of Simulation D where the wave breaking is strong enough to drive an even larger O^+ flux.

The spatial and temporal structure of the GW plays a critical role in the ion upflow response. Fine scale ion motions that result from wave breaking and the mean flow increases from momentum transfer effects in the atmospheric model modulate ion upflow in the topside when compared to a simple GW (such as Simulation A). These GW effects are a natural result of increasing the forcing strength of the GW. The presence of viscous damping, which is the dissipation of GWs by molecular viscosity and thermal conductivity in the thermosphere, and nonlinearity (highly evident in Simulations B and C) acts to deposit momentum into the mean flow, and with the directional orientation of the waves used in this study this results in an increase in the neutral field-aligned velocity. This neutral effect is transferred to the ions as well through ion-neutral drag and increases ion densities above 300 km after ~4:00 UT for Simulations B and C. This density change impacts the total effect of the heating/cooling rates. Wave breaking is another nonlinear GW process that affects the ion response (highly evident in Simulation D and clearly present in Simulation C). More energy is deposited into small-scale wave modes generated by GW breaking; the larger the amplitude of the GW, the quicker and stronger wave breaking occurs. It can generate periods of large field-aligned O^+ velocities, such as 240 m/s at 1,000 km in Simulation D. While this is not at escape speeds, this generates an environment ready for secondary acceleration mechanisms than could produce outflow to the magnetosphere.

This topside transport alters the ion populations available for secondary acceleration processes, such as transverse wave heating, that can lead to outflow into the magnetosphere. Wave heating has been added at 7:30 UT, for a duration of 5 min, to the GWs driving Simulations C and D and increases the O^+ flux during this time by 206% and 107%, respectively. For a baseline comparison the wave heating has also been applied to the control simulation and only raises the O^+ flux from 7.0×10^{11} to 9.5×10^{11} m^{-2} s^{-1}, a percent increase of only 35%. The modulation of the ionosphere by the GW significantly affects the response to secondary acceleration mechanisms such as this transverse wave heating by broadband ELF waves.

While the ISR data from Sondrestrom provided inspiration for the wave parameters used in this study, the data are 1-D in space (along the geomagnetic field line), evolving in time. A phased array, or a scanning mode of the Sondrestrom ISR, has the potential to capture the multidimensional relationships of a GW event and would assist in source determination. Future work may include looking through additional ISR databases to find more GW events; Four very strong neutral wind events were found in the solar cycle 23 search of Sondrestrom's data that yielded the event motivating this study. The commonality of this type of high-latitude, atmosphere-ionosphere interaction can be commented on in future studies.

Acknowledgments

M. R. Burleigh was supported by NSF grant AGS-1255181 and NASA grant NNX14AH07G. M. D. Zettergren was supported by NASA grant NNX15AJ08G. J. B. Snively and C. J. Heale were supported by NSF grant AGS-1151746. The data used in this paper were acquired using the Sondrestrom ISR operated by SRI International for the National Science Foundation and is available at http://isr.sri.com/madrigal/. Wavelet software was provided by C. Torrence and G. Compo and is available at http://atoc.colorado.edu/research/wavelets/. Model simulation data shown in Figures 3–10 are included as files in a zip archive as supporting information and are available in other formats upon request. Eclipse predictions were by Fred Espenak, NASA/GSFC Emeritus.

References

Altadill, D., & Sole, J. (2001). Vertical structure of a gravity wave like oscillation in the ionosphere generated by the solar eclipse of August 11, 1999. *Journal of Geophysical Research*, *106*, 21,419–21,428. https://doi.org/10.1029/2001JA900069

Andre, M., Norqvist, P., Andersson, L., Eliasson, L., Eriksson, A., Blomberg, L., et al. (1998). Ion energization mechanisms at 1700 km in the auroral region. *Journal of Geophysical Research*, *103*, 4199–4222.

Bale, D. S., LeVeque, R. J., Mitran, S., & Rossmanith, J. A. (2003). A wave propagation method for conservation laws and balance laws with spatially varying flux functions. *SIAM Journal on Scientific Computing*, *24*(3), 955–978.

Bertin, F. (1983). Observations of gravity waves in the auroral zone. *Radio Science*, *18*, 1059–1065.

Brambles, O. J., Lotko, W., Zhang, B., Wiltberger, M., Lyon, J., & Strangeway, R. J. (2011). Magnetosphere sawtooth oscillations induced by ionospheric outflow. *Science*, *332*, 1183–1186. https://doi.org/10.1126/science.1202869

Burleigh, M., & Zettergren, M. (2017). Anisotropic fluid modeling of ionospheric upflow: Effects of low-altitude anisotropy and thermospheric winds. *Journal of Geophysical Research: Space Physics*, *122*, 808–827. https://doi.org/10.1002/2016JA023329

Chang, T., Crew, G. B., Hershkowitz, N., Jasperse, J. R., Retterer, J. M., & Winningham, J. D. (1986). Transverse acceleration of oxygen ions by electromagnetic ion cyclotron resonance with broad band left-hand polarized waves. *Geophysical Research Letters*, *13*(7), 636–639. https://doi.org/10.1029/GL013i007p00636

Clark, R. M., Yeh, K. C., & Liu, C. H. (1971). Interaction of internal gravity waves with the ionospheric F2-layer. *Journal of Atmospheric and Terrestrial physics*, *33*(10), 1567–1576.

Crew, G. B., Chang, T., Retterer, J. M., Peterson, W. K., Gurnett, D. A., & Huff, R. L. (1990). Ion cyclotron resonance heated conics: Theory and observations. *Journal of Geophysical Research*, *95*(A4), 3959–3985.

Daglis, I. A., Thorne, R. M., Baumjohann, W., & Orsini, S. (1999). The terrestrial ring current: Origin, formation, and decay. *Reviews of Geophysics*, *37*, 407–438. https://doi.org/10.1029/1999RG900009

David, T. W., Wright, D. M., Milan, S. E., Crowley, S. W. H., Davies, J. A., & McCrea, I. (2018). A study of observations of ionospheric upwelling made by the EISCAT Svalbard Radar during the international polar year campaign of 2007. *Journal of Geophysical Research: Space Physics*, *123*, 2192–2203. https://doi.org/10.1002/2017JA024802

Davis, M. J. (1973). The integrated ionospheric response to internal atmospheric gravity waves. *Journal of Atmospheric and Solar - Terrestrial Physics*, *35*(5), 929–959.

Evans, J. V. (1965). An *F* region eclipse. *Journal of Geophysical Research*, *70*(1), 131–142. https://doi.org/10.1029/JZ070i001p00131

Foster, C., & Lester, M. (1996). Observations of nightside auroral plasma upflows in the F-region and topside ionosphere. *Annales de Geophysique*, *14*, 1274.

Foster, C., Lester, M., & Davies, J. A. (1998). A statistical study of diurnal, seasonal and solar cycle variations of F-region and topside auroral upflows observed by EISCAT between 1984 and 1996. *Annales de Geophysique*, *16*, 1144–1158.

Francis, S. (1973). Acoustic-gravity modes and large-scale traveling ionospheric disturbances of a realistic, dissipative atmosphere. *Journal of Geophysical Research*, *78*, 2278–2301.

Fritts, D. C., & Alexander, M. J. (2003). Gravity wave dynamics and effects in the middle atmosphere. *Reviews of Geophysics*, *41*(1), RG3004. https://doi.org/10.1029/2001RG000106

Fritts, D., Laughman, B., Lund, T., & Snively, J. (2015). Self-acceleration and instability of gravity wave packets: 1. Effects of temporal localization. *Journal of Geophysical Research: Atmospheres*, *120*, 8783–8803. https://doi.org/10.1002/2015JD023363

Fritts, D., & Luo, Z. (1993). Gravity wave forcing in the middle atmosphere due to reduced ozone heating during a solar eclipse. *Journal of Geophysical Research*, *98*, 3011–3021.

Fritts, D., & Vadas, S. (2008). Gravity wave penetration into the thermosphere: Sensitivity to solar cycle variations and mean winds. *Annales de Geophysique*, *26*, 3841–3861.

Ganguli, G., Keskinen, M., Romero, H., Heelis, R., Moore, T., & Pollock, C. (1994). Coupling of microprocesses and macroprocesses due to velocity shear: An application to the low-altitude ionosphere. *Journal of Geophysical Research*, *99*, 8873–8889.

Garcia, K. S., Merkin, V. G., & Hughes, W. J. (2010). Effects of nightside O^+ outflow on magnetospheric dynamics: Results of multifluid MHD modeling. *Journal of Geophysical Research*, *115*, A00J09. https://doi.org/10.1029/2010JA015730

Heale, C. J., Snively, J. B., Hickey, M. P., & Ali, C. J. (2014). Thermospheric dissipation of upward propagating gravity wave packets. *Journal of Geophysical Research: Space Physics*, *119*, 3857–3872. https://doi.org/10.1002/2013JA019387

Hines, C. (1960). Internal atmospheric gravity waves at ionospheric heights. *Canadian Journal of Physics*, *38*, 1441–1481. https://doi.org/10.1139/p60-150

Hocke, K., & Schlegel, K. (1996). A review of atmospheric gravity waves and traveling ionospheric disturbances: 1982–1995. *Annales de Geophysique*, *14*, 917–940.

Hocke, K., Schlegel, K., & Kirchengast, G. (1995). Phases and amplitudes of TIDS in the high-latitude F-region observed by EISCAT. *Journal of Atmospheric and Terrestrial Physics*, *57*, 245–255.

Huba, J. D., Joyce, G., & Fedder, J. A. (2000). SAMI2 is another model of the ionosphere (SAMI2): A new low-latitude ionosphere model. *Journal of Geophysical Research*, *105*, 23,035–23,054. https://doi.org/10.1029/2000JA000035

Hunsucker, R. (1982). Atmospheric gravity waves generated in the high-latitude ionosphere: A review. *Reviews of Geophysics*, *20*, 293–315.

Jordanova, V. K., Kistler, L. M., Kozyra, J. U., Khazanov, G. V., & Nagy, A. F. (1996). Collisional losses of ring current ions. *Journal of Geophysical Research*, *101*, 111–126. https://doi.org/10.1029/95JA02000

Keating, J. G., Mulligan, F. J., & Doyle, D. B. (1990). A statistical study of large field-aligned flows of thermal ions at high-latitudes. *Planet Space Science*, *38*(9), 1187–1201.

Kintner, P. M., Bonnell, J., Arnoldy, R., Lynch, K., Pollock, C., & Moore, T. (1996). SCIFER-transverse ion acceleration and plasma waves. *Geophysical Research Letters*, *23*, 1873–1876.

Kirchengast, G., Hocke, K., & Schlegel, K. (1995). Gravity waves determined by modeling of traveling ionospheric disturbances in incoherent-scatter radar measurements. *Radio Science*, *30*, 1551–1567.

Kirchengast, G., Leitinger, R., & Schlegel, K. (1992). A high-resolution model for the ionospheric F-region at mid-and high-latitude sites. *Annales Geophysicae*, *10*(8), 577–596.

Klumpar, D. (1979). Transversely accelerated ions: An ionospheric source of hot magnetospheric ions. *Journal of Geophysical Research*, *84*, 4229–4237.

Kozyra, J. U., Cravens, T. E., Nagy, A. F., Fontheim, E. G., & Ong, R. S. B. (1984). Effects of energetic heavy ions on electromagnetic ion cyclotron wave generation in the plasmapause region. *Journal of Geophysical Research*, *89*, 2217–2233. https://doi.org/10.1029/JA089iA04p02217

LeVeque, R. J. (1997). Wave propagation algorithms for multidimensional hyperbolic systems. *Journal of Computational Physics*, *131*(2), 327–353.

LeVeque, R. J. (2002). Finite volume methods for hyperbolic problems. Cambridge University Press.

Lennartsson, W., Sharp, R. D., Shelley, E. G., Johnson, R. G., & Balsiger, H. (1981). Ion composition and energy distribution during 10 magnetic storms. *Journal of Geophysical Research*, *86*(A6), 4628–4638. https://doi.org/10.1029/JA086iA06p04628

Liu, C., Horwitz, J., & Richards, P. (1995). Effects of frictional heating and soft-electron precipitation on high-latitude F-region upflows. *Geophysical Research Letters*, *22*, 2713–2716.

Liu, H., & Lu, G. (2004). Velocity shear-related ion upflow in the low-altitude ionosphere. *Annales de Geophysique*, *22*(4), 1149–1153. https://doi.org/10.5194/angeo-22-1149-2004

Lynch, K. A., Semeter, J. L., Zettergren, M., & Kinter, P. (2007). Auroral ion outflow: Low altitude energization. *Annales de Geophysique*, *25*, 1967–1977.

MacDougall, J., & Jayachandran, P. (2011). Solar terminator and auroral sources for traveling ionospheric disturbances in the midlatitude F region. *Journal of Atmospheric and Solar - Terrestrial Physics*, *73*, 2437–2443.

Maeda, S. (1985). Numerical solutions of the coupled equations for acoustic-gravity waves in the upper thermosphere. *Journal of Atmospheric and Terrestrial Physics*, *47*, 965–972.

Moore, T. E. (1991). Origins of magnetospheric plasma. *Reviews of Geophysics*, *29*, 1039.

Moore, T. E., Lundin, R., Alcayde, D., André, M., Ganguli, S. B., Temerin, M., & Yau, A. (1999). Chapter 2-source processes in the high-latitude ionosphere. *Space Science Reviews*, *88*, 7–84.

Nicolls, M. J., & Heinselman, C. J. (2007). Three dimensional measurements of traveling ionospheric disturbances with the poker flat incoherent scatter radar. *Geophysical Research Letters*, *34*, L21104. https://doi.org/10.1029/2007GL031506

Nicolls, M. J., Kelley, M. C., Coster, A. J., Gonzlez, S. A., & Makela, J. J. (2004). Imaging the structure of a large-scale TID using ISR and TEC data. *Geophysical Research Letters*, *31*(9), L09812. https://doi.org/10.1029/2004GL019797

Nicolls, M. J., Vadas, S. L., Aponte, N., & Sulzer, M. P. (2013). Horizontal parameters of daytime thermospheric gravity waves and *E* region neutral winds over Puerto Rico. *Journal of Geophysical Research: Space Physics*, *119*, 575–600. https://doi.org/10.1002/2013JA018988

Nishikawa, K.-I., Ganguli, G. L., Lee, Y. C., & Palmadesso, P. J. (1990). Simulation of electrostatic turbulence due to sheared flows parallel and transverse to the magnetic field. *Journal of Geophysical Research*, *95*, 1029–1038.
Ogawa, Y., Fujii, R., Buchert, S., & Nozawa, S. (2000). Simultaneous EISCAT Svalbard and VHF radar observations of ion upflows at different aspect angles. *Geophysical Research Letters*, *27*, 81–84.
Ogawa, T., Igarashi, K., Aikyo, K., & Maeno, H. (1987). NNSS satellite observations of medium-scale traveling ionospheric disturbances at southern high-latitudes. *Journal of Geomagnetism and Geoelectricity*, *39*, 709–721.
Ogawa, Y., Seki, K., Hirahara, M., Asamura, K., Sakanoi, T., Buchert, S., et al. (2008). Coordinated EISCAT Svalbard radar and Reimei satellite observations of ion upflows and suprathermal ions. *Journal of Geophysical Research*, *113*, A05306. https://doi.org/10.1029/2007JA012791
Picone, J. M., Hedin, A. E., Drob, D. P., & Aikin, A. C. (2002). NRLMSISE-00 empirical model of the atmosphere: Statistical comparisons and scientific issues. *Journal of Geophysical Research*, *107*(A12), 1468. https://doi.org/10.1029/2002JA009430
Retterer, J. M., Chang, T., & Jasperse, J. R. (1983). Ion acceleration in the suprauroral region: A monte carlo model. *Geophysical Research Letters*, *10*(7), 583–586. https://doi.org/10.1029/GL010i007p00583
Richmond, A. (1978). Gravity wave generation, propagation, and dissipation in the thermosphere. *Journal of Geophysical Research*, *83*, 4131–4145.
Sauli, P., Abry, P., Boska, J., & Duchayne, L. (2006). Wavelet characterisation of ionospheric acoustic and gravity waves occurring during the solar eclipse of August 11, 1999. *Journal of Atmospheric and Solar - Terrestrial Physics*, *68*, 586–598.
Semeter, J., Heinselman, C. J., Thayer, J. P., Doe, R. A., & Frey, H. U. (2003). Ion upflow enhanced by drifting F-region plasma structure along the nightside polar cap boundary. *Geophysical Research Letters*, *30*, 2139. https://doi.org/10.1029/2003GL017747
Sharp, R. D., Lennartsson, W., & Strangeway, R. J. (1985). The ionospheric contribution to the plasma environment in near-Earth space. *Radio Science*, *20*(3), 456–462. https://doi.org/10.1029/RS020i003p00456
Shay, M. A., Drake, J. F., Swisdak, M., & Rogers, B. N. (2004). The scaling of embedded collisionless reconnection. *Physics of Plasmas*, *11*, 2199–2213. https://doi.org/10.1063/1.1705650
Shelley, E. G., Johnson, R. G., & Sharp, R. D. (1972). Satellite observations of energetic heavy ions during a geomagnetic storm. *Journal of Geophysical Research*, *77*(31), 6104–6110. https://doi.org/10.1029/JA077i031p06104
Snively, J. B. (2013). Mesospheric hydroxyl airglow signatures of acoustic and gravity waves generated by transient tropospheric forcing. *Geophysical Research Letters*, *40*, 4533–4537. https://doi.org/10.1002/grl.50886
Snively, J. B., & Pasko, V. P. (2008). Excitation of ducted gravity waves in the lower thermosphere by tropospheric sources. *Journal of Geophysical Research*, *113*, A06303. https://doi.org/10.1029/2007JA012693
St-Maurice, J.-P., & Schunk, R. W. (1979). Ion velocity distributions in the high-latitude ionosphere. *Reviews of Geophysics*, *17*(1), 99–134. https://doi.org/10.1029/RG017i001p00099
Strangeway, R. J., Ergun, R. E., Su, Y. J., Carlson, C. W., & Elphic, R. C. (2005). Factors controlling ionospheric outflows as observed at intermediate altitudes. *Journal of Geophysical Research*, *110*, A03221.
Testud, J., & Francois, P. (1971). Importance of diffusion processes in the interaction between neutral waves and ionization. *Journal of Atmospheric and Terrestrial Physics*, *33*(5), 765–774.
Thome, G. D. (1964). Incoherent scatter observations of traveling ionospheric disturbances. *Journal of Geophysical Research*, *69*(19), 4047–4049. https://doi.org/10.1029/JZ069i019p04047
Torrence, C., & Compo, G. (1998). A practical guide to wavelet analysis. *Bulletin of the American Meteorological Society*, *79*(1), 61–78. https://doi.org/10.1175/1520-0477(1998)079<0061:APGTWA>2.0.CO;2
Vadas, S., & Fritts, D. (2005). Thermospheric responses to gravity waves: Influences of increasing viscosity and thermal diffusivity. *Journal of Geophysical Research*, *110*, D15103. https://doi.org/10.1029/2004JD005574
Vadas, S. L., & Nicolls, M. J. (2007). Using PFISR measurements and gravity wave dissipative theory to determine the neutral, background thermospheric winds. *Geophysical Research Letters*, *35*, L02105. https://doi.org/10.1029/2007GL031522
Vlasov, A., Kauristie, K., van de Kamp, M., Luntama, J.-P., & Pogoreltsev, A. (2011). A study of traveling ionospheric disturbances and atmospheric gravity waves using EISCAT Svalbard radar IPY-data. *Annales Geophysicae*, *29*, 2101–2116. https://doi.org/10.5194/angeo-29-2101-2011
Wahlund, J.-E., & Opgenoorth, H. J. (1989). EISCAT Observations of strong ion outflows from the F-region ionosphere during auroral activity: Preliminary results. *Geophysical Research Letters*, *16*(7), 727–730. https://doi.org/10.1029/GL016i007p00727
Wahlund, J.-E., Opgenoorth, H. J., Häggström, I., Winser, K. J., & Jones, G. O. L. (1992). EISCAT observations of topside ionospheric ion outflows during auroral activity: Revisited. *Journal of Geophysical Research*, *97*(A3), 3019–3037.
Whalen, B. A., Bernstein, W., & Daly, P. W. (1978). Low altitude acceleration of ionospheric ions. *Geophysical Research Letters*, *5*(1), 55–58. https://doi.org/10.1029/GL005i001p00055
Whalen, B., Watanabe, S., & Yau, A. (1991). Thermal and suprathermal ion observations in the low altitude transverse ion energization region. *Geophysical Research Letters*, *18*, 725–728.
Yokoyama, T., Hysell, D. L., Otsuka, Y., & Yamamoto, M. (2009). Three-dimensional simulation of the coupled Perkins and E_s-layer instabilities in the nighttime midlatitude ionosphere. *Journal of Geophysical Research*, *114*, A03308. https://doi.org/10.1029/2008JA013789
Yoshida, N., Watanabe, S., Fukunishi, H., Sakanoi, T., Mukai, T., Hayakawa, H., et al. (1999). Coordinated Akebono and EISCAT observations of suprathermal ion outflow in the nightside inverted-V region. *Journal of Atmospheric and Solar - Terrestrial Physics*, *62*, 449–465.
Yu, Y., & Ridley, A. J. (2013). Exploring the influence of ionospheric o^+ outflow on magnetospheric dynamics: The effect of outflow intensity. *Journal of Geophysical Research: Space Physics*, *118*, 5522–5531. https://doi.org/10.1002/jgra.50528
Zeng, W., & Horwitz, J. L. (2008). Storm enhanced densities (SED) as possible sources for cleft ion fountain dayside ionospheric outflows. *Geophysical Research Letters*, *35*, L04103. https://doi.org/10.1029/2007GL032511
Zeng, W., Horwitz, J. L., & Tu, J.-N. (2006). Characteristic ion distributions in the dynamic auroral transition region. *Journal of Geophysical Research*, *111*, A04201. https://doi.org/10.1029/2005JA011417
Zettergren, M., Lynch, K., Hampton, D., Nicolls, M., Wright, B., Conde, M., et al. (2014). Auroral ionospheric F region density cavity formation and evolution: MICA campaign results. *Journal of Geophysical Research: Space Physics*, *119*, 3162–3178. https://doi.org/10.1002/2013JA019583
Zettergren, M., & Semeter, J. (2012). Ionospheric plasma transport and loss in auroral downward current regions. *Journal of Geophysical Research*, *117*, A06306. https://doi.org/10.1029/2012JA017637
Zettergren, M., & Snively, J. (2013). Ionospheric signatures of acoustic waves generated by transient tropospheric forcing. *Geophysical Research Letters*, *40*, 5345–5349. https://doi.org/10.1002/2013GL058018
Zettergren, M. D., & Snively, J. B. (2015). Ionospheric response to infrasonic-acoustic waves generated by natural hazard events. *Journal of Geophysical Research: Space Physics*, *120*, 8002–8024. https://doi.org/10.1002/2015JA021116